Sulfur-Modified Graphitic Carbon Nitride Nanostructures as an Efficient Electrocatalyst for Water Oxidation

Vinayak S. Kale, Uk Sim, Jiwoong Yang, Kyoungsuk Jin, Sue In Chae, Woo Je Chang, Arun Kumar Sinha, Heonjin Ha, Chan-Cuk Hwang, Junghyun An, Hyo-Ki Hong, Zonghoon Lee, Ki Tae Nam, and Taeghwan Hyeon**

There is an urgent need to develop metal-free, low cost, durable, and highly efficient catalysts for industrially important oxygen evolution reactions. Inspired by natural geodes, unique melamine nanogeodes are successfully synthesized using hydrothermal process. Sulfur-modified graphitic carbon nitride (S-modified g-CN_x) electrocatalysts are obtained by annealing these melamine nanogeodes in situ with sulfur. The sulfur modification in the g-CN_x structure leads to excellent oxygen evolution reaction activity by lowering the overpotential. Compared with the previously reported nonmetallic systems and well-established metallic catalysts, the S-modified g-CN_x nanostructures show superior performance, requiring a lower overpotential (290 mV) to achieve a current density of 10 mA cm^{-2} and a Tafel slope of 120 mV dec^{-1} with long-term durability of 91.2% retention for 18 h. These inexpensive, environmentally friendly, and easy-to-synthesize catalysts with extraordinary performance will have a high impact in the field of oxygen evolution reaction electrocatalysis.

1. Introduction

Oxygen evolution reaction (OER) has been a main focus of scientists working in the field of energy harvesting to convert water into oxygen. The importance of OER lies in the mechanisms of catalytic oxygen evolution for clean and sustainable fuel cells, rechargeable metal–air batteries, and solar fuel production (water splitting). Traditionally, OER has been catalyzed by expensive, rare earth metals, such as Ru and Ir (oxide).[1] Inexpensive metal/metal oxide composites,

V. S. Kale, Dr. J. Yang, S. I. Chae, Dr. A. K. Sinha, Prof. T. Hyeon
Center for Nanoparticle Research
Institute for Basic Science (IBS)
Seoul 08826, Republic of Korea
E-mail: thyeon@snu.ac.kr

V. S. Kale, Dr. J. Yang, S. I. Chae, Dr. A. K. Sinha, Prof. T. Hyeon
School of Chemical and Biological Engineering and
Institute of Chemical Processes
Seoul National University
Seoul 08826, Republic of Korea

Dr. U. Sim, Dr. J. Yang, Dr. K. Jin, W. J. Chang, H. Ha, J. An, Prof. K. T. Nam
Department of Materials Science and Engineering
Research Institute of Advanced Materials (RIAM)
Seoul National University
Seoul 08826, Republic of Korea
E-mail: nkitae@snu.ac.kr

W. J. Chang
Interdisciplinary Program for Bioengineering
Seoul National University
Seoul 08826, Republic of Korea

Dr. C.-C. Hwang
Beamline Research Division
Pohang Accelerator Laboratory
POSTECH
Pohang 37673, Republic of Korea

H.-K. Hong, Prof. Z. Lee
School of Materials Science and Engineering
Ulsan National Institute of Science and Technology
Ulsan 44919, Republic of Korea

DOI: 10.1002/smll.201603893

including Co, Mn, Fe, and Ni-based systems, have been used as alternatives, but low conductivity limits their practical applications.[2–11] Great efforts have been made to find alternatives based on nonmetal systems, particularly carbon-based nanomaterials.[12–15] Graphitic carbon nitride (g-C_3N_4) is reported to exhibit good electrocatalytic activities originating from the pyridinic and pyrrolic nitrogen in the carbon framework, and has been successfully used as supports or composite materials in many catalytic or photocatalytic reactions.[16–27] Moreover, the low production cost, high thermal and chemical stability, environmental harmlessness, and easy scalability of g-C_3N_4 have attracted increasing attention in recent years.[28–44] To increase the conductivity or catalytic properties of g-C_3N_4, various strategies have been developed, such as nanostructuring,[45–50] making composites with other conducting carbon materials,[51–58] and doping or modification with heteroatom such as P,[22,35] B,[23,44] I,[59,60] F,[61] and S.[62–66] Although the heteroatom modified/mediated structures are not well defined and the exact position of dopant is not well understood yet, the enhancement of photocatalytic activity in g-C_3N_4 nanostructures is significant.[44,59,67] OER is considered to be a complicated process involving four-electron transfer with a sluggish reaction rate that always suffers from a high overpotential, leading to huge energy losses in practical applications. Though some g-C_3N_4 nanomaterials have been reported to be OER active, achieving low overpotentials in the OER process is still a great challenge.[33,35,68,69]

Herein, sulfur-modified g-CN_x nano-electrocatalysts were successfully synthesized from melamine nanogeodes (MNGs) by in situ modification with sulfur and subsequent annealing. The unique MNGs were synthesized by a very simple hydrothermal method, inspired by the synthesis and morphology of natural geodes. S-modified g-CN_x nanostructures show excellent OER activity with the lowest overpotential of 290 mV at a current density of 10 mA cm^{-2}. Moreover, a long durability of 91.2% retention for 18 h is achieved, which is essential for electrocatalysts. This result is, to date, the best performance realized among nonmetal-based electrocatalysts. The modification of g-CN_x nanostructures with sulfur greatly reduces the overpotential for the OER process and results in an efficient electrocatalyst with long-term durability.

2. Results and Discussion

2.1. Synthesis and Characterization of Electrocatalysts

Unique MNGs were used as starting materials for the synthesis of g-CN_x nanostructures and S-modified g-CN_x nanostructures. The synthesis and morphology of MNGs is inspired by natural geodes found in the earth's crust, which are formed under high temperature and pressure in liquids (**Figure 1**a). To achieve similar reaction conditions, a hydrothermal method, which is a well-established, simple, and cost-effective method, is used to synthesize MNGs from cheap melamine in environmentally friendly aqueous medium. The stepwise synthesis of MNGs in solution is shown schematically in Figure 1b (i–iv). After the hydrothermal reaction, MNGs are obtained by centrifugation of the reaction mixture. Owing to their lower density, MNGs remain in the upper fraction, which is carefully separated from the residue. The MNGs can be acquired as a powder by evaporating the solvent. Low-magnification transmission electron microscope (TEM) image in Figure 1c shows the morphology of the MNGs. The high-resolution transmission electron microscope (HRTEM) images in Figure 1d,e show that the MNGs are multiwalled with polygonal shapes, similar to natural geodes. The MNGs are ≈10–20 nm in diameter and each nanogeode has a closed-cage structure with 8–10 multilayers and an interlayer spacing of 0.336 nm. To obtain S-modified g-CN_x nanostructures, typically 0.5 g sulfur powder is mixed thoroughly with 1.0 g MNG powder using a mortar and pestle, and then the mixture is annealed in argon atmosphere. In the absence of sulfur, g-CN_x nanostructures are produced in a similar way. Under similar conditions, two-step thermal annealing of commercial melamine without formation of MNGs results in the synthesis of bulk g-CN_x, which is used as the reference sample. The S-modified g-CN_x nanostructures were further characterized by TEM elemental analysis (**Figure 2**). For comparison, the g-CN_x nanostructures without sulfur were similarly analyzed (Figure S1, Supporting Information). As shown in the TEM and HRTEM images, the morphologies of the S-modified g-CN_x nanostructures (Figure 2a,b) and the g-CN_x nanostructures (Figure S1a,b, Supporting Information) are similar, which implies that sulfur modification does not affect the morphology. High-angle annular dark field scanning TEM combined with electron energy loss spectroscopy (EELS) was used to characterize the elemental distribution in S-modified g-CN_x nanostructures (Figure 2c). The spatial distributions of the various elements were visualized by EELS mapping based on the intensity variation of the energy loss peaks (Figure 2d). The EELS spectrum of the area marked with a red box in Figure 2c clearly shows an S-*L* edge along with C-*K* and N-*K* edges. The C-*K* edge shows one π^* state at 284.75 eV and one σ^* state at 292 eV. The N-*K* edge shows combined π^* and σ^* states at 403 eV. The peak observed at 165.7 eV due to the S-$L_{2,3}$ edge is not observed in the spectrum for g-CN_x nanostructures without sulfur-modification (see Figure S1c,d of the Supporting Information for comparison). This significant EELS elemental peak, along with the elemental mapping images shown in Figure 2e–g for the C-*K* edge, N-*K* edge, and S-$L_{2,3}$ edge spectra, respectively, clearly indicate the presence of sulfur in S-modified g-CN_x nanostructures. Whereas elemental mapping image of g-CN_x nanostructures is shown in Figure S1e,f (Supporting Information) for the C-*K* edge, N-*K* edge spectra, respectively, Figure S1g (Supporting Information) for S-$L_{2,3}$ edge spectra shows noise level. The synthesis and graphitic nature of carbon nitride is also confirmed by high resolution synchrotron powder diffraction (HRPD) analysis of bulk g-CN_x, g-CN_x nanostructures, and S-modified g-CN_x nanostructures. The HRPD spectra in **Figure 3**a show two prominent peaks. The strong peak at $2\theta = 26.5°$ arises from the (002) interlayer diffraction of the fundamental carbon nitride structure ($d = 0.326$ nm), whereas the second peak at $2\theta = 12.5°$ is considered to correspond to the in-plane repeating units of tri-*s*-triazine ($d = 0.663$ nm). Furthermore, the chemical nature and bonding structures

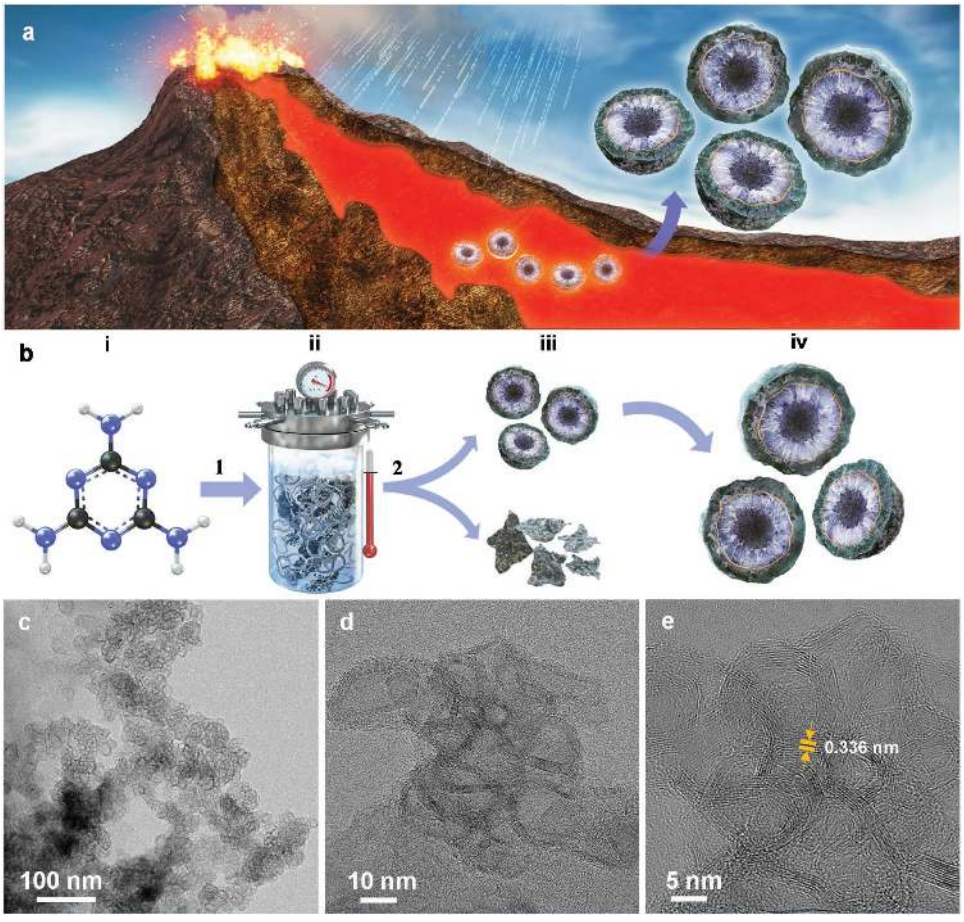

Figure 1. Synthesis of melamine nanogeodes. a) Schematic representation of the synthesis process for naturally occurring geodes in the earth's crust. b) The precursor melamine (i) in an aqueous solution is used to synthesize melamine nanogeodes (MNGs) under the hydrothermal conditions of 160 °C for 24 h in step (1). After completion of the hydrothermal reaction, the reaction mixture (ii) of MNGs mixed with a residue is centrifuged in step (2) to separate the lighter density MNGs from the higher density residue (iii). Representative images of MNGs (iv). c) TEM image of MNGs. d,e) HRTEM images of MNGs showing multiwalled closed cage structures with an interlayer distance of 0.336 nm.

of the g-CN_x materials were investigated by Fourier transform infrared (FT-IR) spectroscopy, as shown in Figure 3b. The sharp peak at 810 cm^{-1} is corresponded to the breathing mode of the tri-*s*-triazine units. The multiple bands observed in the range of 900–1800 cm^{-1} are typical of the CN heterocyclic structures present in the carbon nitride structure. The broad peak at 2900–3600 cm^{-1} is an enhanced adsorption due to N—H stretches. The C, N, and S elements in the S-modified g-CN_x nanostructures are characterized by X-ray photoelectron spectroscopy (XPS), and the widescan XPS spectra are shown in Figure 3c. The C1s core-level XPS data of S-modified g-CN_x nanostructures in Figure 3d shows two peaks centered at 284.5 and 287.7 eV. The first peak at 284.5 eV is due to sp^2 C—C bonds and the peak at 287.7 eV is due to sp^2 bonded carbon with N in aromatic rings (N—C=N). The N1s core-level XPS data of S-modified g-CN_x nanostructures in Figure 3e show four peaks centered at 398.3, 399.9, 400.5, and 403.7 eV. The intense peak at 398.3 eV is due to the sp^2 bonded N from the triazine rings (C—N=C), and 399.9 eV for tertiary nitrogen [N— $(C)_3$], the peak at 400.5 eV is for amino functional groups (C—N—H) and the peak at 403.7 eV is due to charging effect. The peaks centered at 163.1 and 164.2 eV shown in Figure 3f for S2p core-level XPS data are assigned for S—C bonds, which implies the interaction of sulfur and carbon atoms of the g-CN_x planes.[29,62,65] The details of XPS data for bulk g-CN_x and g-CN_x nanostructures is given in Figure S3 (Supporting Information) and comparison of XPS analysis is given in Table S1 (Supporting Information).

2.2. OER Activity of the Electrocatalysts

To investigate the electrocatalytic activity of the g-CN_x nanoelectrocatalysts, cyclic voltammetry was measured using a rotating disk electrode (RDE) system. The current density versus potential (*J*–*E*) curves (**Figure 4**a) obtained from the RDE measurements show that the current density associated with the OER exponentially increases when the potential is swept from 1.0 to 1.95 V versus Reversible Hydrogen Electrode (RHE). To compare the capability of these materials for OER activity, the potential required to attain a current density of 10 mA cm^{-2} for the OER is defined as overpotential from *J*–*E* curves (Figure 4c; Table S2, Supporting Information). In addition, RDE measurements of a bulk g-CN_x catalyst as a standard reference sample were obtained. The overpotential to attain a current density of 10 mA cm^{-2} for

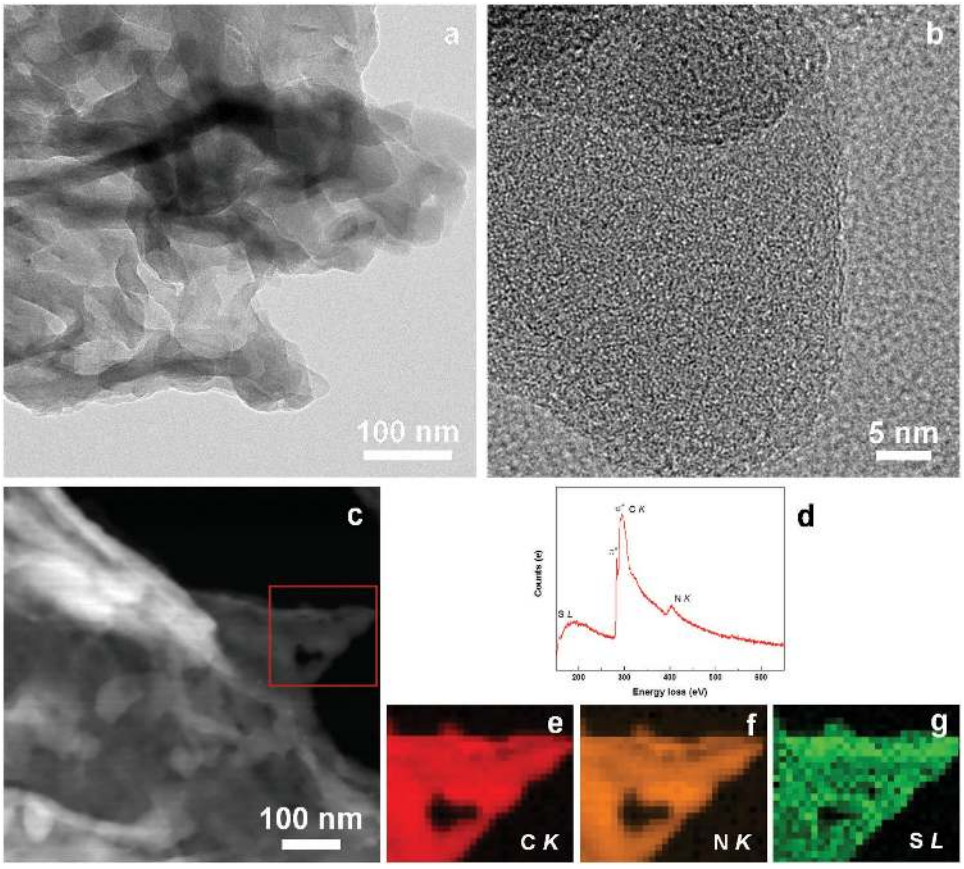

Figure 2. Electron microscopy characterization of S-modified g-CN_x nanostructures. a) TEM and b) HRTEM images, respectively. c) High-angle annular dark field scanning TEM image. d) EELS spectra collected at the site indicated in (c). e–g) EELS elemental maps obtained from the site indicated by the red box in c: e) C-*K* edge, f) N-*K* edge, and g) S-$L_{2,3}$ edge.

the OER with g-CN_x nanostructures is 480 mV versus RHE; this potential is negatively (cathodically) shifted by 200 mV relative to that for the bulk g-CN_x catalyst. The OER properties of the g-CN_x nanostructures are further enhanced by sulfur modification. Tuning and optimization of the amount of S-modification allows the OER activity to be increased by lowering the overpotential (Figure 4a; Figure S4, Supporting Information). Interestingly, the *J*–*E* curve for the S-modified g-CN_x nanostructures shows the largest negative shift with an overpotential at 10 mA cm^{-2} of 290 mV versus RHE, indicating a negative shift of 190 mV compared with that of unmodified g-CN_x nanostructures. To the best of our knowledge, this value is the lowest among g-CN_x OER catalysts reported to date and is comparable to those of the best-performing metal-based catalysts (see Table S2, Supporting Information). We varied the amount of initial sulfur (0.125, 0.25, 0.5, and 1.0 g) with 1.0 g of MNG to tune sulfur loading of the electrocatalysts and confirmed that the elemental composition of sulfur is 0.18, 0.24, 0.29, and 0.32 at%, respectively (Table S1, Supporting Information). The electrocatalytic performance exhibits dependency on the initial amount of sulfur used. The overpotentials (η) are 380, 320, 290, and 300 mV for the electrocatalysts prepared using 0.125, 0.25, 0.5, and 1.0 g of sulfur, respectively (Figure S4, Supporting Information). The best performance (η = 290 mV) is achieved for the electrocatalyst prepared using 0.5 g of sulfur, designated as S-modified g-CN_x nanostructures. The S-mediated bulk g-CN_x catalyst has been synthesized in the same way, except that commercial melamine is used instead of MNG powder. The lower activity of S-mediated bulk g-CN_x catalysts shows the importance of MNGs for the synthesis of the electrocatalyst (Figure S5, Supporting Information). We also varied annealing temperature during calcination step for the synthesis of S-modified g-CN_x nanostructures and confirmed the sample annealed at 600 °C showed the best OER activity (Figure S6, Supporting Information).

To measure an electrochemically active surface area (ECSA), a capacitance of an electrical double layer (C_{dl}) at a solid/electrolyte interface was evaluated by measuring the *J*–*E* response of the g-CN_x nanostructures and the S-modified g-CN_x nanostructures on the glassy carbon electrode at various scan rates (Figure S8, Supporting Information). The C_{dl} is estimated from the slope of the plot of J_C, which is the current at the potential with a net current density of 0 μA cm^{-2} increasing the scan rate from 20 to 100 mV s^{-1}. The capacitance is 237.5 μF cm^{-2} for S-modified g-CN_x nanostructures and 145.0 μF cm^{-2} for g-CN_x nanostructures, respectively. Values are much higher than that of typical compact flat electrode reported to date (10–20 μF cm^{-2}).[70] The slope is also proportional to the exchange current density, which is directly related to the catalytically active surface area.[71,72] The ECSA is calculated from the C_{dl} divided by the

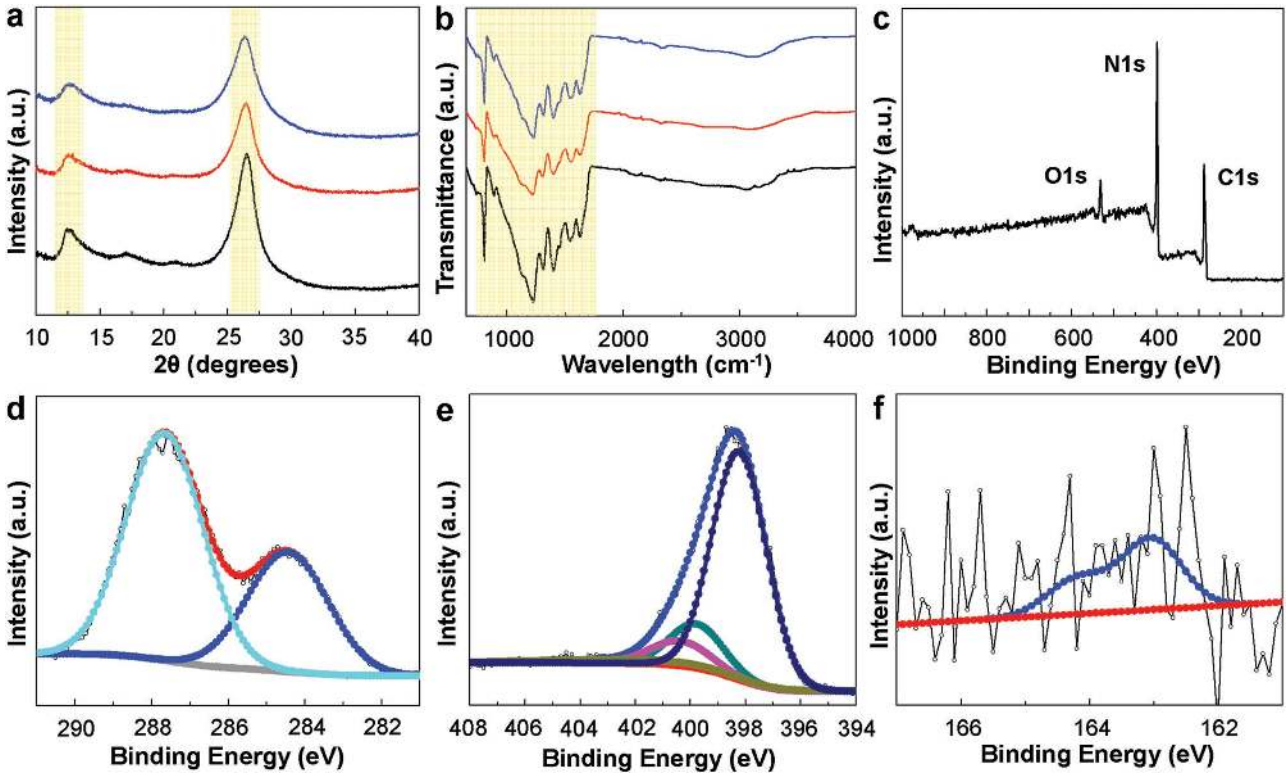

Figure 3. Structural characterization of electrocatalysts. Comparisons of a) HRPD and b) FT-IR spectra of bulk g-CN_x (black), g-CN_x nanostructures (red), and S-modified g-CN_x nanostructures (blue). c) Widescan XPS spectra, d) C1s, e) N1s, and f) S2p XPS spectra of S-modified g-CN_x nanostructures.

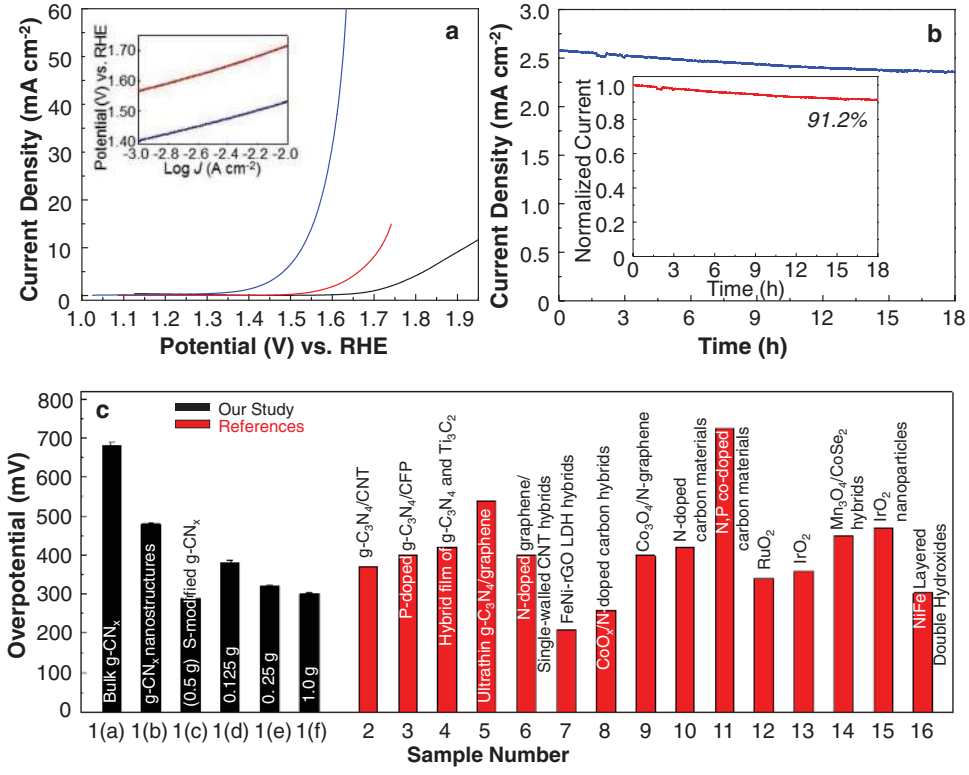

Figure 4. Electrochemical response of g-CN_x catalysts. a) Current density–potential (*J*–*E*) curves for bulk g-CN_x (black), g-CN_x nanostructures (red), and S-modified g-CN_x nanostructures (blue). The inset shows the Tafel plots derived from the *J*–*E* data. b) Chronoamperometric operation of S-modified g-CN_x nanostructures at the potential of 1.45 V versus RHE. The inset shows the normalized current density with increasing operation time. c) Overpotentials of various catalyst samples at 10 mA cm^{-2}. Detailed information about the various catalysts can be found in Table S2 (Supporting Information).

capacitance of a smooth planar surface of the catalyst (C_s). Using the general C_s value of μF cm^{-2} = 40 in 1 M KOH,[2] the ECSA of the S-modified g-CN_x nanostructures and g-CN_x nanostructures are 1.16 and 0.71 cm^2, which corresponds to the roughness factor of 5.94 and 3.63, respectively. Therefore, the S-modified g-CN_x nanostructures have high electrochemical catalytic surface area, due to the sulfur atoms adsorbed on the g-CN_x surface, which may also provide the effective active sites for the OER. Furthermore, the rotating ring disk electrode measurement shows that the oxygen is directly generated from S-modified g-CN_x nanostructures (Figure S9, Supporting Information).

The superior catalytic performance of S-modified g-CN_x nanostructures is further demonstrated by their high stability. Chronoamperometry measurements were performed at 1.45 V versus RHE in 1 M KOH solution (pH 14), and the obtained current densities normalized by their initial values are displayed as a function of time in Figure 4b. The S-modified g-CN_x nanostructures maintain a current density of 2.3 mA cm^{-2} and more than 91% of the normalized current, even after 18 h, which is comparable to other g-CN_x-based OER catalysts reported to date (Table S3, Supporting Information). This result indicates that the S-modified g-CN_x nanostructures exhibit good stability as well as efficient electrocatalytic activity toward the OER, demonstrating the significance of the sulfur modification in the g-CN_x catalyst.

To gain more quantitative insight into the catalytic activity of the g-CN_x catalysts, the *J*–*E* curves in Figure 4a are converted into Tafel plots, in which the potential is plotted as a function of the logarithm of *J*. Owing to solution resistance at the interface between the electrode and electrolyte, the measured potentials compensate for ohmic potential drop (iR) losses. The Tafel slope is defined as the potential required to increase the resulting current by one order of magnitude. A Tafel slope of 146 mV dec^{-1} is obtained for the g-CN_x nanostructures, whereas a Tafel slope of 120 mV dec^{-1} is obtained for the S-modified g-CN_x nanostructures (Figure 4a, inset). The Tafel slope is an inherent property of the catalyst that is determined by the rate-limiting step for the OER. Theoretically, Tafel slope value is closely related to the transfer coefficient value, α, that can provide mechanical insights for OER. Tafel slope of 60–80 mV dec^{-1} is corresponding to 2.3 RT/F which means that reversible one-electron transfer reaction takes place before rate-determining step. Tafel slope of 110–130 mV dec^{-1}, 2.3 × 2RT/F suggests that a single-electron transfer step without pre-equilibrium step should exist in the following four electron-involved stepwise reaction paths

$$H_2O(l) + {}^* \rightarrow HO^* + H^+ + e^- \quad (1)$$

$$HO^* \leftrightarrow O^* + H^+ + e^- \quad (2)$$

$$O^* + H_2O(l) \leftrightarrow HOO^* + H^+ + e^- \quad (3)$$

$$HOO^* \leftrightarrow {}^* + O_2(g) + H^+ + e^- \quad (4)$$

where * is an active site for OER catalysis. Therefore, observed Tafel slope of 120 mV dec^{-1} in S-modified g-CN_x nanostructures implies that the rate determining step is determined by a single-electron transfer step as shown in Equation (1).

To evaluate the detailed water oxidation mechanism, proton reaction order was further investigated by a pH

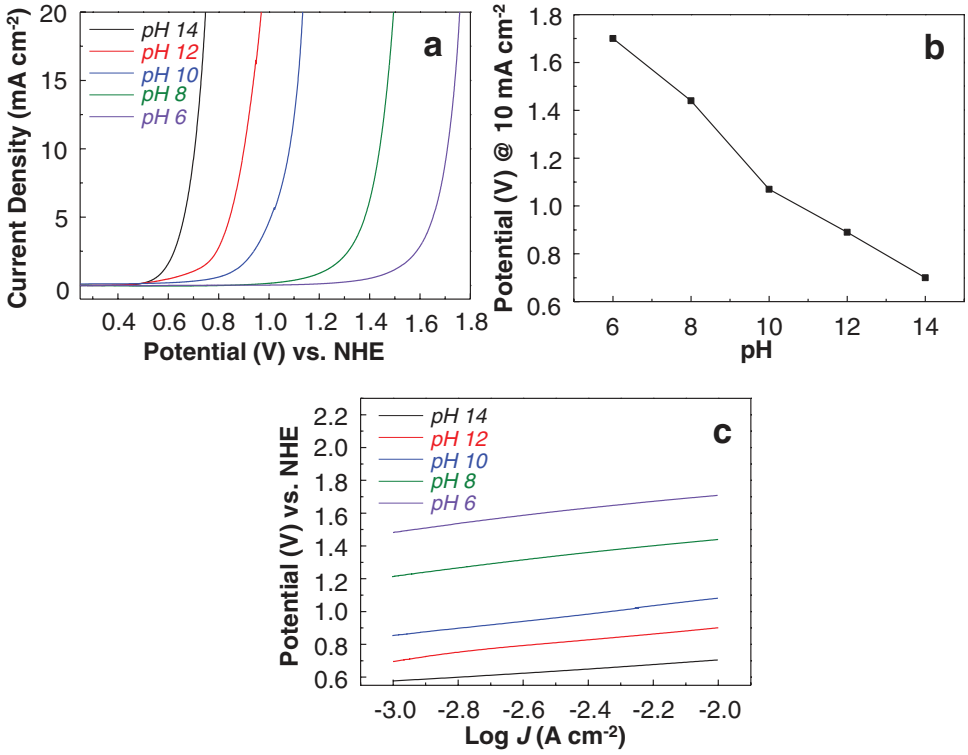

Figure 5. pH dependence of S-modified g-CN_x nanostructures. a) *J*–*E* curves of S-modified g-CN_x nanostructures in a pH range from 6 to 14. b) Potential of the catalyst at 10 mA cm^{-2} with increasing pH. c) Tafel plots derived from the *J*–*E* data in (a).

dependency test in the pH range between 6 and 14. The dependence of proton activity on current density is derived as

$$\left(\frac{\partial E}{\partial \mathrm{pH}}\right)_j = -\left(\frac{\partial \log j}{\partial \mathrm{pH}}\right)_E \left(\frac{\partial E}{\partial \log j}\right)_{\mathrm{pH}} \quad (5)$$

From the pH dependency test, $\left(\frac{\partial E}{\partial \mathrm{pH}}\right)_j$ is calculated as –127.5 mV pH^{-1} (**Figure 5**a,b). Substituting the value of $\left(\frac{\partial E}{\partial \mathrm{pH}}\right)_j$ and the Tafel slope $\left(\frac{\partial E}{\partial \log j}\right)_{\mathrm{pH}}$ (Figure 5c) into Equation (5) gave a $\left(\frac{\partial \log j}{\partial \mathrm{pH}}\right)_E$ value of 1.06. It indicates that the water oxidizing reaction rate is affected by the proton activity with inverse first-order dependence. Taken together, the electrochemical law for S-modified g-CN_x nanostructures is derived, as follows

$$i = k_0 (a_{\mathrm{H}^+})^{-1.06} \mathrm{e}^{\frac{0.5EF}{\mathrm{RT}}} \quad (6)$$

where k_0, a_{H^+}, and F are a potential-independent constant, the proton activity, and the Faraday constant, respectively. From the established Equation (6), it can be assumed that a single electron is involved at the rate-determining step, as obtained from the above described experimental results.

From the literature, the OER mechanism of g-CN_x has also been calculated, and the rate determining step is shown to be the first step. Modification with sulfur does not change the OER mechanism, but lowers the overpotential for the OER, which is consistent with the experimental results. Density Functional Theory (DFT) calculation from the literature also can provide helpful insights for possible intrinsic mechanism for the enhanced OER property of the S-modified g-CN_x nanostructures.[64] The S-doping or S-adsorption of g-CN_x forms the material a conductor by reasonably narrowing of the band gap and also by the Fermi level shifting to the conduction band. The electronic structure of g-CN_x catalyst in our system might be also affected by S-modification favorable to enhanced conductivity as well as higher catalytic property. The impedance spectroscopy was also analyzed to measure a resistance of catalysts in an electrolyte solution. The resistances of the bare glassy carbon electrode, bulk g-CN_x, g-CN_x nanostructures, and S-modified g-CN_x nanostructures are 7.0, 10.0, 7.3, and 7.1 Ω, respectively. The resulting lower resistance also proves that the S-modified g-CN_x nanostructures have higher conductivity compared to the bare g-CN_x nanostructures. To investigate more about the origin of the enhanced catalytic activity, electrochemical impedance measurements were performed. A Nyquist plot of a typical impedance result with only one semicircle is shown in Figure S10a (Supporting Information). The single semicircle indicates that the equivalent circuit for the electrocatalysis is characterized by one time constant. Compared with the bare g-CN_x nanostructures (135 Ω cm^2), the semicircle observed for the S-modified g-CN_x nanostructures is much smaller, corresponding to a lower charge-transfer resistance (38 Ω cm^2). The charge-transfer resistance is related to the kinetic barrier energy for Faradaic reactions (OER) across the interface between the catalyst and electrolyte.[73] The charge-transfer resistance is also inversely proportional to the exchange current for the Faradaic reaction, as described by the Butler–Volmer equation.[74] Consequently, the lower charge-transfer resistance of the S-modified g-CN_x nanostructures promotes the OER, thus lowering the overpotential. Moreover, the dependence of the phase angle on the frequency (Bode phase plot), as shown in Figure S10b (Supporting Information), shows the same frequency time constant trend. Thus, the impedance analysis verifies the enhanced catalytic properties of the S-modified g-CN_x nanostructures and the above-mentioned mechanism.

3. Conclusion

In conclusion, we successfully synthesized S-modified g-CN_x nanostructures by in situ modification of our novel melamine nanogeodes with sulfur and they showed excellent catalytic properties due to minimization of the activation energy for the OER. The low overpotential (η = 290 mV) achieved with the S-modified g-CN_x nanostructures is indeed an urgent requirement for OER catalysts to minimize energy loss during the process. To date, this value is the best among non-metal, metal/metal oxide, and well-established catalysts. The long-term performance of 18 h with more than 91% retention of activity for S-modified g-CN_x nanostructures will allow realization of practical applications. New catalysts are needed for the OER, and the unique morphology MNGs to achieve g-CN_x nanostructures and improved activity through sulfur modification will attract much attention in this field. The developed synthetic strategy and our understanding can be directly applied to various other electrocatalysts, emphasizing the importance of nanostructure and sulfur modification for better activity and stability.

4. Experimental Section

Materials: Melamine and sulfur were purchased from Sigma-Aldrich and used as received.

Synthesis of Melamine Nanogeodes: Novel MNGs were synthesized by a simple hydrothermal method. Typically, 0.5 g melamine was dissolved in 75 mL of deionized water at a slightly higher temperature of 50 °C. After dissolution of melamine, the solution was transferred to a 100 mL Teflon-lined stainless steel autoclave. An electric oven was used to heat the autoclave for 24 h at 160 °C. After completion of the reaction, the reaction mixture was allowed to cool naturally to room temperature. The reaction product was carefully collected and centrifuged at 10 000 rpm for 30 min. The upper fraction was assumed to contain the MNGs and was collected. The MNGs were recovered in powder form by evaporating the water with a rotavapor.

Synthesis of Graphitic Carbon Nitride Nanostructures: The g-CN_x nanostructures were prepared using 1.0 g of the MNG powder obtained using the above procedure. Two-step heating of the powder in a high-quality alumina crucible with a lid was conducted under an argon atmosphere at a gas flow rate of 100 sccm. In the first step, the powder was heated from room temperature to 400 °C at a heating rate of 4.4 °C min^{-1} and held for 1 h 30 min.

In the second step, the powder was further heated to 600 °C at the same heating rate of 4.4 °C min^{-1} and held for 2 h. After the heating procedure, the sample was allowed to cool naturally to room temperature, and the final product was collected as g-CN_x nanostructures in powder form.

Synthesis of Sulfur-Modified Graphitic Carbon Nitride Nanostructures: S-modified g-CN_x nanostructures in powder form were prepared using 0.5 g of sulfur and 1.0 g of MNG powder, thoroughly mixed with a mortar and pestle followed by the two-step heating process described above. Various S-modified g-CN_x catalysts were obtained by varying the initial amount of sulfur (0.125, 0.25, 0.5, or 1.0 g) to 1 g of MNG powder.

Synthesis of Bulk Graphitic Carbon Nitride: Bulk graphitic carbon nitride was prepared by using 1.0 g commercial melamine as a precursor and the two-step heating process described above. The final product was collected as bulk graphitic carbon nitride in powder form.

Electrochemical Cell Preparation and Measurements: The preparation procedure for the working electrode was as follows. The catalyst ink was prepared using g-CN_x catalyst, carbon black (Super P), and polyvinylidene fluoride (8:1:1) in *N*-methyl-2-pyrrolidone. The catalyst ink (10 µL) was deposited on a glassy carbon tip (5 mm diameter) and dried at 120 °C. The electrochemical measurements were performed in a three-electrode cell using an electrochemical analyzer (CHI 760E, CH Instruments, Inc.). A Pt ring was used as the counter electrode, and an Ag/AgCl/3 M NaCl electrode was used as the reference electrode. A graphite counter electrode was also used and the CV response result was same as the CV response using Pt counter electrode (Figure S11, Supporting Information). The electrodes were evaluated from pH 6 to 12 in phosphate buffered saline solution buffered using KOH, and from pH 12 to 14 in aqueous KOH and $NaClO_4$ buffered using KOH. The ionic strength of all electrolytes was maintained at 1 M. The reference electrode was carefully calibrated with respect to RHE at 25 °C. The RHE was calibrated to –0.201 V versus the Ag/AgCl reference electrode. Electrode potential was converted to the Normal Hydrogen Electrode (NHE) scale, using the following equation: E(NHE) = E(Ag/AgCl) + 0.201 V. For the electrochemical study, a RDE system was used (PINE Inc.) with a glass carbon tip (5 mm diameter). The RDE measurements were performed at a rotation speed of 2000 rpm and a scan rate of 5 mV s^{-1}. The current densities were obtained based on the geometry surface area of the working electrode in the electrolyte (0.196 cm^2 for the glassy carbon tip). The measured potentials were corrected for the iR losses that originated from the resistance of the interface between the substrate and the electrolyte. Resistances were measured using iR compensation mode in the electrochemical analyzer.

Physicochemical Characterizations: TEM analysis was performed using an aberration-corrected TEM (Titan G2 Cube 60–300 kV, FEI). The samples were mounted on Quantifoil mesh grids. To minimize exposure of the sample to the beam, the image was collected at a low operating voltage (80 kV) with a least beam exposure approach. The scanning transmission electron microscopy imaging and EELS mapping were carried out on an FEI Titan cubed G2 electron microscope operated at 80 kV equipped with a monochromator. A probe size of 1.5 nm and a best energy resolution of 0.2 ± 0.05 eV, as measured from the full-width-at-half-maximum of the zero-loss peak, were achieved. For simultaneous EELS mapping of the *K*-edge structures for carbon and nitrogen, and *L*-edge structure for sulfur, a 5 mm spectrometer entrance aperture and 0.25 eV per channel dispersion were used. Synchrotron HRPD measurements were performed at the 9B beamline of Pohang Accelerator Laboratory (PAL, Pohang, Republic of Korea), the incident X-ray source was vertically collimated by mirror and monochromatized to λ = 1.4863 Å by a double-crystal Si(111) monochromator. XPS analyses were performed in a Ultra-High Vacuum (UHV) multipurpose surface analysis system (Sigma Probe, Thermo, UK) operating at base pressures $<10^{-9}$ mbar, and the HRPES end-station at 10D beamline of PAL. FT-IR spectra were collected using a TENSOR27/Bruker instrument. Tristar II 3020Micromeritics (USA) was used to measure Brunauer-Emmett-Teller (BET) surface area.

Supporting Information

Supporting Information is available from the Wiley Online Library or from the author.

Acknowledgements

V.S.K. and U.S. contributed equally to this work. The authors acknowledge financial support from the Institute for Basic Science in the Republic of Korea (IBS-R006-D1) (T.H.), the Global Frontier R&D Program on Center for Multiscale Energy System (2011-0031571) funded by the Ministry of Science, ICT & Future, Korea through the Research Institute of Advanced Materials (RIAM) and by KIST Institutional Program (0543-20160004) (K.T.N.), the financial support by the NRF through the SRC Center for Topological Matter (No. 2011-0030787), the experiments at PLS were supported in part by MSIP and POSTECH (C.-C.H.), and the National Research Foundation of Korea (NRF) grant funded by the Korean government (MSIP) (No. 2015R1A2A2A01006992) (Z.L.).

[1] L. Trotochaud, S. W. Boettcher, *Scr. Mater.* **2014**, *74*, 25.
[2] C. C. L. McCrory, S. Jung, J. C. Peters, T. F. Jaramillo, *J. Am. Chem. Soc.* **2013**, *135*, 16977.
[3] C. C. L. McCrory, S. Jung, I. M. Ferrer, S. M. Chatman, J. C. Peters, T. F. Jaramillo, *J. Am. Chem. Soc.* **2015**, *137*, 4347.
[4] H. Kim, J. Park, I. Park, K. Jin, S. E. Jerng, S. H. Kim, K. T. Nam, K. Kang, *Nat. Commun.* **2015**, *6*, 8253.
[5] K. Jin, A. Chu, J. Park, D. Jeong, S. E. Jerng, U. Sim, H. Y. Jeong, C. W. Lee, Y. S. Park, K. D. Yang, G. K. Pradhan, D. Kim, N. E. Sung, S. H. Kim, K. T. Nam, *Sci. Rep.* **2015**, *5*, 10279.
[6] K. Jin, J. Park, J. Lee, K. D. Yang, G. K. Pradhan, U. Sim, D. Jeong, H. L. Jang, S. Park, D. Kim, N. E. Sung, S. H. Kim, S. Han, K. T. Nam, *J. Am. Chem. Soc.* **2014**, *136*, 7435.
[7] T. Takashima, K. Hashimoto, R. Nakamura, *J. Am. Chem. Soc.* **2012**, *134*, 18153.
[8] T. Takashima, K. Hashimoto, R. Nakamura, *J. Am. Chem. Soc.* **2012**, *134*, 1519.
[9] A. Yamaguchi, R. Inuzuka, T. Takashima, T. Hayashi, K. Hashimoto, R. Nakamura, *Nat. Commun.* **2014**, *5*, 4256.
[10] B. J. Trześniewski, O. Diaz-Morales, D. A. Vermaas, A. Longo, W. Bras, M. T. M. Koper, W. A. Smith, *J. Am. Chem. Soc.* **2015**, *137*, 15112.

[11] N. Han, F. Zhao, Y. Li, *J. Mater. Chem. A* **2015**, *3*, 16348.
[12] Y. Zhao, R. Nakamura, K. Kamiya, S. Nakanishi, K. Hashimoto, *Nat. Commun.* **2013**, *4*, 2390.
[13] Y. Jia, L. Zhang, A. Du, G. Gao, J. Chen, X. Yan, C. L. Brown, X. Yao, *Adv. Mater.* **2016**, *28*, 9532.
[14] J. Li, Y. Wang, T. Zhou, H. Zhang, X. Sun, J. Tang, L. Zhang, A. M. Al-Enizi, Z. Yang, G. Zheng, *J. Am. Chem. Soc.* **2015**, *137*, 14305.
[15] H. Wu, J. Geng, H. Ge, Z. Guo, Y. Wang, G. Zheng, *Adv. Energy Mater.* **2016**, *6*, 1600794.
[16] X. Wang, K. Maeda, A. Thomas, K. Takanabe, G. Xin, J. M. Carlsson, K. Domen, M. Antonietti, *Nat. Mater.* **2009**, *8*, 76.
[17] X. Chen, J. Zhang, X. Fu, M. Antonietti, X. Wang, *J. Am. Chem. Soc.* **2009**, *131*, 11658.
[18] Y. Wang, J. Yao, H. Li, D. Su, M. Antonietti, *J. Am. Chem. Soc.* **2011**, *133*, 2362.
[19] J. Liu, H. Wang, M. Antonietti, *Chem. Soc. Rev.* **2016**, *45*, 2308.
[20] Y. Zheng, J. Liu, J. Liang, M. Jaroniec, S. Z. Qiao, *Energy Environ. Sci.* **2012**, *5*, 6717.
[21] Y. Zheng, Y. Jiao, M. Jaroniec, Y. Jin, S. Z. Qiao, *Small* **2012**, *8*, 3550.
[22] Y. Zhang, T. Mori, J. Ye, M. Antonietti, *J. Am. Chem. Soc.* **2010**, *132*, 6294.
[23] Y. Wang, H. Li, J. Yao, X. Wang, M. Antonietti, *Chem. Sci.* **2011**, *2*, 446.
[24] J. Shui, M. Wang, F. Du, L. Dai, *Sci. Adv.* **2015**, *1*, e1400129.
[25] G. Wu, Y. Hu, Y. Liu, J. Zhao, X. Chen, V. Whoehling, C. Plesse, G. T. M. Nguyen, F. Vidal, W. Chen, *Nat. Commun.* **2015**, *6*, 7258.
[26] K. Sakaushi, M. Antonietti, *Acc. Chem. Res.* **2015**, *48*, 1591.
[27] S. J. A. Moniz, S. A. Shevlin, D. J. Martin, Z. X. Guo, J. Tang, *Energy Environ. Sci.* **2015**, *8*, 731.
[28] J. Zhang, J. Sun, K. Maeda, K. Domen, P. Liu, M. Antonietti, X. Fu, X. Wang, *Energy Environ. Sci.* **2011**, *4*, 675.
[29] J. Xu, S. Cao, T. Brenner, X. Yang, J. Yu, M. Antonietti, M. Shalom, *Adv. Funct. Mater.* **2015**, *25*, 6265.
[30] Y. Zheng, Y. Jiao, J. Chen, J. Liu, J. Liang, A. Du, W. Zhang, Z. Zhu, S. C. Smith, M. Jaroniec, G. Q. Lu, S. Z. Qiao, *J. Am. Chem. Soc.* **2011**, *133*, 20116.
[31] J. Liang, Y. Zheng, J. Chen, J. Liu, D. H. Jurcakova, M. Jaroniec, S. Z. Qiao, *Angew. Chem., Int. Ed.* **2012**, *51*, 3892.
[32] Y. Zheng, Y. Jiao, Y. Zhu, L. H. Li, Y. Han, Y. Chen, A. Du, M. Jaroniec, S. Z. Qiao, *Nat. Commun.* **2014**, *5*, 3783.
[33] T. Y. Ma, S. Dai, M. Jaroniec, S. Z. Qiao, *Angew. Chem., Int. Ed.* **2014**, *53*, 7281.
[34] Y. Jiao, Y. Zheng, M. Jaroniec, S. Z. Qiao, *Chem. Soc. Rev.* **2015**, *44*, 2060.
[35] T. Y. Ma, J. Ran, S. Dai, M. Jaroniec, S. Z. Qiao, *Angew. Chem., Int. Ed.* **2015**, *54*, 4646.
[36] S. Cao, J. Low, J. Yu, M. Jaroniec, *Adv. Mater.* **2015**, *27*, 2150.
[37] L. B. Sun, X. Q. Liu, H. C. Zhou, *Chem. Soc. Rev.* **2015**, *44*, 5092.
[38] Y. Gong, M. Li, Y. Wang, *ChemSusChem* **2015**, *8*, 931.
[39] Z. Zhao, Y. Sun, F. Dong, *Nanoscale* **2015**, *7*, 15.
[40] Y. Zheng, L. Lin, B. Wang, X. Wang, *Angew. Chem., Int. Ed.* **2015**, *54*, 12868.
[41] J. Zhang, Y. Chen, X. Wang, *Energy Environ. Sci.* **2015**, *8*, 3092.
[42] X. Dong, F. Cheng, *J. Mater. Chem. A* **2015**, *3*, 23642.
[43] Y. Zhao, J. Zhang, L. Qu, *ChemNanoMat* **2015**, *1*, 298.
[44] Z. Lin, X. Wang, *Angew. Chem., Int. Ed.* **2013**, *52*, 1735.
[45] J. S. Lee, G. S. Park, S. T. Kim, M. Liu, J. Cho, *Angew. Chem., Int. Ed.* **2013**, *52*, 1026.
[46] H. Huang, S. Yang, R. Vajtai, X. Wang, P. M. Ajayan, *Adv. Mater.* **2014**, *26*, 5160.
[47] J. Sun, J. Zhang, M. Zhang, M. Antonietti, X. Fu, X. Wang, *Nat. Commun.* **2012**, *3*, 1139.
[48] Z. Zhou, J. Wang, J. Yu, Y. Shen, Y. Li, A. Liu, S. Liu, Y. Zhang, *J. Am. Chem. Soc.* **2015**, *137*, 2179.
[49] T. Y. Ma, Y. Tang, S. Dai, S. Z. Qiao, *Small* **2014**, *10*, 2382.
[50] S. Yang, Y. Gong, J. Zhang, L. Zhan, L. Ma, Z. Fang, R. Vajtai, X. Wang, P. M. Ajayan, *Adv. Mater.* **2013**, *25*, 2452.
[51] G. Vilé, D. Albani, M. Nachtegaal, Z. Chen, D. Dontsova, M. Antonietti, N. López, J. Pérez-Ramírez, *Angew. Chem., Int. Ed.* **2015**, *54*, 11265.
[52] J. Liu, W. Li, L. Duan, X. Li, L. Ji, Z. Geng, K. Huang, L. Lu, L. Zhou, Z. Liu, W. Chen, L. Liu, S. Feng, Y. Zhang, *Nano Lett.* **2015**, *15*, 5137.
[53] Y. Hou, Z. Wen, S. Cui, X. Feng, J. Chen, *Nano Lett.* **2016**, *16*, 2268.
[54] Q. Pang, L. F. Nazar, *ACS Nano* **2016**, *10*, 4111.
[55] L. Hao, J. Ning, B. Luo, B. Wang, Y. Zhang, Z. Tang, J. Yang, A. Thomas, L. Zhi, *J. Am. Chem. Soc.* **2015**, *137*, 219.
[56] J. Zhu, K. Sakaushi, G. Clavel, M. Shalom, M. Antonietti, T. P. Fellinger, *J. Am. Chem. Soc.* **2015**, *137*, 5480.
[57] Y. Hou, F. Zuo, A. P. Dagg, J. Liu, P. Feng, *Adv. Mater.* **2014**, *26*, 5043.
[58] J. Liu, Y. Liu, N. Liu, Y. Han, X. Zhang, H. Huang, Y. Lifshitz, S. T. Lee, J. Zhong, Z. Kang, *Science* **2015**, *347*, 970.
[59] G. Zhang, M. Zhang, X. Ye, X. Qiu, S. Lin, X. Wang, *Adv. Mater.* **2014**, *26*, 805.
[60] Q. Han, C. Hu, F. Zhao, Z. Zhang, N. Chen, L. Qu, *J. Mater. Chem. A* **2015**, *3*, 4612.
[61] Y. Wang, Y. Di, M. Antonietti, H. Li, X. Chen, X. Wang, *Chem. Mater.* **2010**, *22*, 5119.
[62] G. Liu, P. Niu, C. Sun, S. C. Smith, Z. Chen, G. Q. Lu, H. M. Cheng, *J. Am. Chem. Soc.* **2010**, *132*, 11642.
[63] S. Lin, X. Ye, X. Gao, J. Huang, *J. Mol. Catal. A: Chem.* **2015**, *406*, 137.
[64] S. Stolbov, S. Zuluaga, *J. Phys. Condens. Matter* **2013**, *25*, 085507.
[65] C. Xu, Q. Han, Y. Zhao, L. Wang, Y. Li, L. Qu, *J. Mater. Chem. A* **2015**, *3*, 1841.
[66] J. Hong, X. Xia, Y. Wang, R. Xu, *J. Mater. Chem.* **2012**, *22*, 15006.
[67] Y. Wang, J. Zhang, X. Wang, M. Antonietti, H. Li, *Angew. Chem., Int. Ed.* **2010**, *49*, 3356.
[68] J. Tian, Q. Liu, A. M. Asiri, K. A. Alamry, X. Sun, *ChemSusChem* **2014**, *7*, 2125.
[69] T. Y. Ma, J. L. Cao, M. Jaroniec, S. Z. Qiao, *Angew. Chem., Int. Ed.* **2016**, *55*, 1138.
[70] J. P. Randin, E. Yeager, *J. Electrochem. Soc.* **1971**, *118*, 711.
[71] D. Kong, H. Wang, Z. Lu, Y. Cui, *J. Am. Chem. Soc.* **2014**, *136*, 4897.
[72] S. Trasatti, O. A. Petrii, *J. Electroanal. Chem.* **1992**, *327*, 353.
[73] D. Merki, H. Vrubel, L. Rovelli, S. Fierro, X. Hu, *Chem. Sci.* **2012**, *3*, 2515.
[74] A. J. Bard, L. R. Faulkner, *Electrochemical Methods: Fundamentals and Applications*, Wiley, New York **1980**.

Received: November 22, 2016
Revised: January 21, 2017
Published online: February 20, 2017